Journal of Astronomical Telescopes, Instruments, and Systems

AstronomicalTelescopes.SPIEDigitalLibrary.org

Lynx x-ray optics based on thin monolithic shells: design and development

Marta M. Civitani
Giancarlo Parodi
Gabriele Vecchi
Mauro Ghigo
Stefano Basso
Jacqueline M. Davis
Ronald F. Elsner
Kilaru Kiranmayee
Giovanni Pareschi
Douglas Swartz
Giorgio Toso

SPIE.

Marta M. Civitani, Giancarlo Parodi, Gabriele Vecchi, Mauro Ghigo, Stefano Basso, Jacqueline M. Davis, Ronald F. Elsner, Kilaru Kiranmayee, Giovanni Pareschi, Douglas Swartz, Giorgio Toso, "Lynx x-ray optics based on thin monolithic shells: design and development," *J. Astron. Telesc. Instrum. Syst.* **5**(2), 021014 (2019), doi: 10.1117/1.JATIS.5.2.021014.

Lynx x-ray optics based on thin monolithic shells: design and development

Marta M. Civitani,[a,*] Giancarlo Parodi,[b] Gabriele Vecchi,[a] Mauro Ghigo,[a] Stefano Basso,[a] Jacqueline M. Davis,[c] Ronald F. Elsner,[c] Kilaru Kiranmayee,[c] Giovanni Pareschi,[a] Douglas Swartz,[c] and Giorgio Toso[d]
[a]National Institute of Astrophysics, Astronomical Observatory of Brera, Merate, Italy
[b]BCV Progetti, Milano, Italy
[c]Marshall Space Flight Center, Huntsville, Alabama, United States
[d]National Institute for Astrophysics, IASF, Milano, Italy

Abstract. Lynx is the future x-ray observatory with superb imaging capabilities (<1 arc sec half-energy width) and large throughput (2 m^2 effective area @ 1 keV), which is being considered in the U.S. to take over Chandra. The implementation of the x-ray mirror module represents a very challenging aspect, and different approaches are being considered. Thin and low-weight substrates, working in grazing incidence configuration, are necessary to meet the severe mass constraints, but they have to also preserve the requirement of an excellent angular resolution. The use of monolithic glass (fused silica) shells is an attractive solution, provided that their thickness is kept very small [<4 mm for mirror shells up of 3-m diameter]. We present the optomechanical design of the Lynx mirror assembly based on this approach, together with the ongoing technological development process. In particular, we discuss the figuring process, which is based on direct polishing followed by an ion-beam figuring correction. A temporary structure is specifically devoted to support the shell during the figuring and polishing operations and to manage the handling of the shell through all phases up to integration into the final telescope supporting spoke wheel. The results achieved so far on a prototype shell will be discussed. [DOI: 10.1117/1.JATIS.5.2.021014]

Keywords: x-ray telescopes; monolithic shells; optomechanical design; fused silica; Bonnet polishing; ion-beam figuring.

Paper 18117SS received Nov. 20, 2018; accepted for publication Apr. 12, 2019; published online May 10, 2019.

1 Introduction

The Lynx design is based on an x-ray telescope with an unprecedented combination of superb angular resolution, wide field of view (FOV), and large effective area.[1,2] The Lynx mirror assembly (LMA) relies on grazing incidence optics working in the 0.15 to 10 keV energy range. The LMA focal length and the outer diameter are 10 m and 3 m, respectively, allowing for maximum flexibility in the choice of launch vehicle and fairing size. The LMA requirements are summarized in Table 1.

The Lynx high-angular resolution requirement was established in the 1990s for the optics of the Chandra X-ray Observatory (formerly AXAF).[3] Chandra is flying four full-shell mirror pairs with an exquisite angular resolution of <0.5 arc sec half-energy width (HEW), but provides a relatively modest effective area at 1 keV (~0.11 m^2). The mirrors were 1.6- to 2.4-cm thick made of Zerodur. They were fabricated by combining a very accurate metrology and standard grinding and polishing techniques. The LMA will require at least an order of magnitude thinner mirror substrates without degrading the high-angular resolution. As thin and lightweight mirrors are inherently not stiff, the extremely tight error margins will be a technical challenge, either during the production steps or for in-flight operation.

To meet the Lynx requirements, multiple x-ray mirror technologies are under study. The adjustable segmented x-ray optics approach is based on piezo actuators deposited directly on the backside of the slumped glass segments. Furthermore, semiconductor strain gauges can be deposited directly on the piezoelectric cells. The strain can be correlated to local mirror bending and the calibration data used for on-orbit figure monitoring and correction.[4] Lightweight mirrors can be realized using the grind-and-polish process on monocrystalline silicon segments. Extremely thin, flat silicon wafers are usually polished to highest figure and finish quality in the semiconductor industry. The silicon wafer-manufacturing process has been adapted for making x-ray mirrors and a mounting concept based on meta-shell is proposed.[5]

The "full shell" concept is based on the grinding, polishing, superpolishing, and final ion-beam figuring correction of thin monolithic glass mirror shells (MSs). The shells are made of fused silica, a relatively cheap material but with adequate mechanical and thermal properties. The shells are very thin compared to the diameter: the thickness foreseen for a 3-m diameter shell is <4 mm. In this way, it is possible to increase the number of the shells, and therefore, the effective area, limiting the weight of the whole optics. The realization of these thin mirrors is possible by taking advantage of the intrinsic stiffness of the monolithic axis-symmetric shells and adopting an *ad hoc* integration concept based on a shell-supporting structure (S3) jig to be used for the handling and to support the shell in all the manufacturing steps.[6]

In this paper we present this last "full shell" concept. We discuss the preliminary optical design of the mirror assembly (Sec. 2), the material selection (Sec. 3), the shell-supporting scheme (Sec. 4), the manufacturing process steps (Sec. 5), the integration process and the mirror module mechanical design (Sec. 6). The top-level error budget is presented in Sec. 7.

*Address all correspondence to Marta M. Civitani, E-mail: marta.civitani@inaf.it

Table 1 Requirements for the LMA.

Parameter	Requirement
HEW (on axis)	0.5 arc sec
Effective area (on-axis, 1 keV)	>2 m^2
FOV diameter	20 arc min
Grasp (HEW < 1″, $E = 1$ keV)	>600 $m^2 \times arc\,min^2$
Maximum diameter	3 m
Focal length	10 m
MM weight	2000 kg (+500 kg margin)

The results of the test carried out on prototypal shells are summarized in Sec. 8, while Sec. 9 describes the future plans for the technology maturation. Conclusions are stated in Sec. 10.

2 Optical Design

Given the monolithic structure of the shells and the large diameter to account for, their thickness is a trade-off between the mechanical requirements and the optical performances. To limit the weight of the whole optics, the walls should be very thin compared to the diameter. This allows for growing the number of the shells and therefore the effective area. On the other hand, too thin MS, being too floppy, encounters structural problems, making all issues related to MS deformations more severe.

In the current design, the thickness for a 0.15-m diameter shell is 1.5 mm. It increases linearly with the radius up to 3.4 mm for a 3-m diameter shell. As shown in the next paragraphs, these values are sustainable from the mechanical point of view. Further reduction of maximum shell thickness would have positive impact in the mirror module (MM) weight. This option could be chosen once a complete characterization of the glass strength will be available.

The MM design foresees that the primary and secondary reflecting surfaces composing a MS (front and rear surfaces) are separated and fixed to a spoke wheel (SW) in the region of the intersection plane (IP) (Fig. 1). This configuration is the best choice for several reasons. (1) It reduces the problems during MS manufacturing as there is no need for grinding and polishing the area between the primary and the secondary surfaces in correspondence to the IP. Indeed, if the two surfaces are adjacent, the accessibility to this area would be limited and a nonreflecting area, of at least some millimeters, should be envisaged. (2) Moreover, the alignment of the two optical axes may be optimized during the integration phase and the best angular position can be precisely tuned in order to compensate the fabrication errors on the primary and the secondary surfaces. (3) From the programmatic point of view, two separated surfaces allow the parallelization of the manufacturing process. This is particularly important for larger shells, with higher grinding and polishing time. (4) From the mechanical point of view, the MS have higher natural frequencies, given the shorter length. (5) The mass distribution in the MM structure is more balanced, with better performances in terms of frequencies and gravity load effects. In particular, this configuration is advantageous in lateral gravity condition, which is currently foreseen for on-ground calibration.

The preliminary optical design is generated taking into account the requirements reported in Table 1. The LMA has been designed in Wolter–Schwarzchild (WS) configuration,[7] to obtain the best angular performances in the FOV. From a general point of view, longer shells offer better area-to-mass ratio and concur to the reduction of the total number of shells to be realized. On the contrary, the requirement on the optical performances in the FOV introduces limitation into the geometrical configuration of the shells, in particular with respect to the maximum length of the shell. The maximum MS length increases linearly with the radius. Given the limit in angular resolution at the edges of the FOV, the maximum height of the shell is fixed for each diameter. The larger shells can be longer, whereas the innermost one needs to be shorter. The greater is the required FOV, the shorter the shells need to be. For example, taking into account a 0.5″ margin [to be distributed between the thermomechanical (T/M), manufacturing and integration contributions], the HEW limit at the edge of the FOV reduces from 1″ to 0.85″. To fulfill this limit, the length of the mirror shells ranges between 50.1 and 497.9 mm.

With respect to the selection of innermost shell diameter, the contribution to the effective area of the innermost shells is relevant only at high x-ray energy (≫1 keV): with the current thickness selection, these shells are not really useful for increasing the effective area at low energy. On the other hand, as they contribute to the requirement of 6 to 8 keV, their geometry is modified with respect to the WS prescription in order to improve their area-to-mass ratio. In particular, the minimum shell length is fixed to 150 mm, as the optical performances in the FOV of the innermost shells will be in any case limited, given the different curvature of their focal plane with respect to the larger shells. The shells with smaller diameter present a focal plane with some millimeters of curvature. Instead, the outer shells have an almost flat focal plane. The optimization of the focal plane needs to be carried out taking into account the collecting area contribution at low energies and, therefore, will follow the geometry required for larger shells. Moreover, given that the theoretical required length of the innermost shells is quite small (around 140 mm in total), longer shells will concur to overcome manufacturing problems.

Further constraints have been fixed. The minimum diameter of the innermost shells has been fixed to 400 mm, with some margin on the accessibility with grinding and polishing existing equipment. Further reduction in the diameter may be taken into account with custom-designed machines. In principle, the separation of innermost shells is a fraction of a millimeter. It has been increased to 1 mm to allow a safety margin during the integration phase, but it could be reduced if needed.

As anticipated, the optical design foresees detached primary and secondary mirror surfaces, integrated to form the complete LMA in a common SW structure. The connection with the LMA structure is realized only on one of the sides of the primary or secondary surface shell, in order to avoid over-constraint. The primary mirror surface is integrated on the smaller diameter side, whereas the secondary surface is connected on the larger diameter side. Taking into account the size of the optics, their weight, and the preliminary mechanical design of the structure, the distance between the primary and the secondary MSs is set to 280 mm, constant for all the shells. Further optimizations are possible and will be evaluated in future. The current optical design for the LMA foresees 164 shells. The thickness ranges between 1.6 and 3.4 mm, whereas the length of the semishell is

between 157.9 and 348.2 mm. The weight of the shells ranges between 1.36 and 46.2 kg, with a total mirror mass of 1890.7 kg (assuming glass density).

In accordance with WS design, the MSs are distributed shifted along the optical axis on a spherical surface in order to satisfy the Abbe sine condition. The optical design started from the innermost shells, adapting the focal length in order to guarantee the focal plane overlapping. The shift in the MS is maximum for outermost shells and is around 125 mm. From the structural point of view, this curvature of the spider is advantageous. Assuming a lightweight structure made of silicon carbide or carbon fiber reinforced polymer (CFRP), the weight of the spider is estimated to be around 300 kg.

Two different reflecting coatings have been considered in the effective area theoretical evaluation. In the first case a layer of 40-nm iridium ($\sigma = 0.5$ nm) is considered, whereas in the second, a layer of platinum with an overcoat of carbon (40 nm Pt + 10 nm C, $\sigma = 0.5$ nm) is assumed. At 1 keV, the Pt + C performs better than the others up to 2.1 deg, whereas the reflectivity of the Ir is higher for angles above 0.4 deg at 7 keV. Therefore, the overall effective area at different energies can be improved with the selection of the coating in dependence of the radius of the shell. Moreover, different optimizations of the multilayer coating recipes could be envisaged.

The number of shells and their radial positions are defined based on the total mirror weight and the effective area reached. The shell does not completely fill the available radial space and there is some margin for the optimization of the shell distribution. In particular, there are five radial gaps in correspondence of the SW radial connections needed to reinforce the structure. The effective area reached by the whole mirror assembly as a function of the photon energy is shown in Fig. 2. The effective area at 1 keV is around 2 m^2 (with 11% obscuration from the structure already taken into account).

The optical performances in the FOV have been evaluated for the LMA with ray-tracing software, taking into account the reflectivity of the surface in dependence of the energy and the incidence angle of the impinging rays. The difference in the focal plane curvature turns out in a general dependence the focal plane curvature with the energy, as it is directly related to the effective area at different energies of the shells. For off-axis angles, >5 arc min, the curved focal plane is indispensable to limit the optical performance degradation.

The optimization of the optical performances in the FOV is finalized by placing the common focal plane in the position

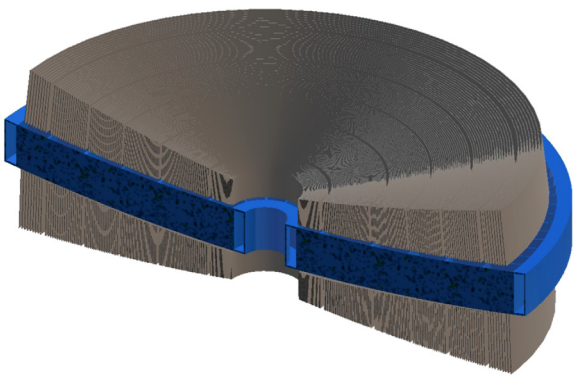

Fig. 1 Mirror assembly configuration: a single spoke is placed between the primary and the secondary shell sections.

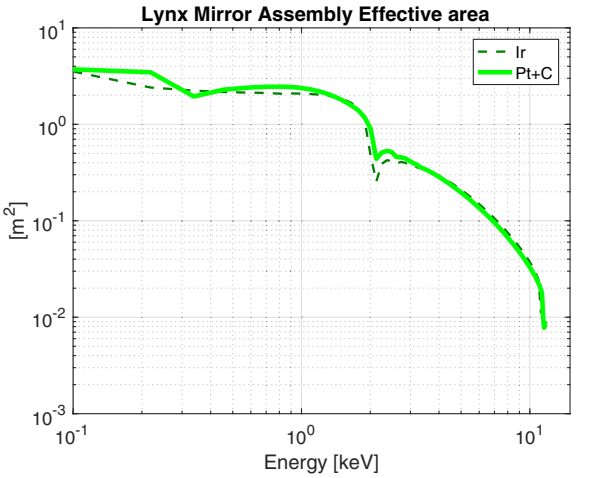

Fig. 2 LMA effective area in the 0.1- to 12-keV range. About 40 nm Ir coating or 40 nm Pt + 10 nm C are considered.

corresponding to the middle of the FOV (5′ arc min). This choice degrades the optical performances on axis to 0.3″ but improve the off-axis behavior from 1.6″ to 1.3″ at the edge of the FOV. It is particularly important to increase the GRASP, as the requirement is defined by taking into account 1″ HEW limit and 10 arc min off-axis angle. The overall HEW of the LMA, in the assumption of a curved focal plane, is shown at the bottom of Fig. 3. The vignetting function is determined at different energies with ray-tracing software considering the ray passages at the different interfaces. The results are calculated up to 12 arc min and are shown in Fig. 3.

The corresponding GRASP is calculated taking into account variable limits in the HEW (between 1″ and 2″ HEW) and variable size of the FOV (between 10 and 12 arc min). The results are shown in Fig. 4, together with the required value of 600 $m^2 \times arc\,min^2$. If determined within a FOV of 10 arc min and considering values of HEW <1 arc sec, the total grasp is slightly below the requirements. The grasp requirement is reached by increasing the maximum value for the HEW to 1.2 arc sec. Further optimization will be considered in next phases.

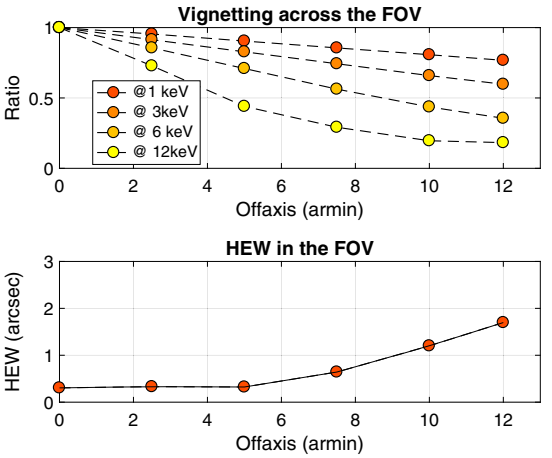

Fig. 3 The vignetting for off-axis directions up to 12 arc min at1 keV, 3 keV, 6 keV, and 12 keV. On the bottom panel the HEW at 1 keV is shown for the same off-axis directions.

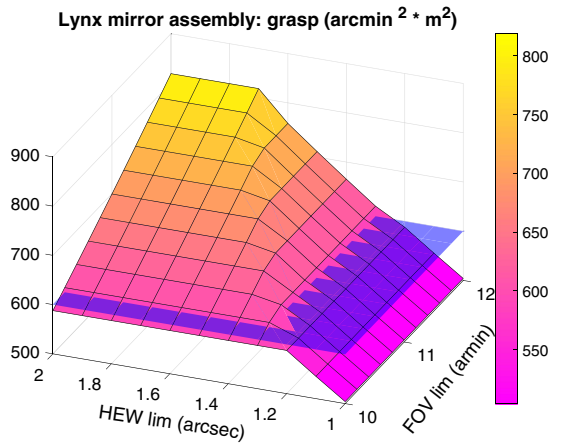

Fig. 4 The GRASP in function of the FOV considered in the calculation and of the limiting HEW.

Fig. 5 A cylindrical tube of fused silica before the grinding to generate a double-conical configuration.

3 Materials Selection

As anticipated, fused silica is a cost-effective solution for the MS realization. It is a synthetic molten, high purity, and noncrystalline quartz glass. The T/M properties of the material (in particular its low density and high Young's modulus) are suitable to reach the necessary stiffness once the proper and optimized procedures are used. The coefficient of thermal expansion (CTE) is very low, so that it can hold up very high thermal loads. Therefore, this material is very competitive with respect to Zerodur or ULE glasses, as the procurement cost of fused silica is lower.

Raw, fused silica tubes are currently available on the market at affordable costs. The Heraeus Quarzglas GmbH & Co KG normally produces fused silica tubes with diameters up to 900 mm and wall thicknesses between 0.5 and 13 mm. In past years, we have already purchased several raw quartz tubes from Heraeus Quarzglas GmbH & Co KG. Starting from a cylindrical shape, they were ground to a double-cone configuration, with a two-step grinding procedure. The external and internal surfaces of the glass tubes are both machined by means of a row grinding process. Higher diameters can be achieved with the hot slumping technique: this is feasible and has been demonstrated by Heraeus with small prototypes. This process, traditionally used for resizing the cylindrical tubes, can be optimized to change from cylindrical configuration to the conical one. This would significantly reduce the amount of material to be removed in raw grinding especially for larger shell. Starting from the conical fused silica shell, first grinding operations are performed to obtain the required thickness with tolerances of a few tens of microns with respect to the final conical shape. As stated, the process has already been tested for shell with diameters up to 600 mm: a cylindrical tube of fused silica before the grinding to double-conical shape is shown in Fig. 5.

Corning Incorporated (USA) may also provide fused silica shells and the realization of very large diameter shell (up to 3 m) is already in the company capabilities. In this case the shells are cut via water-jet from a chunk of fused silica and then grinded. The outermost shell lengths are of the order of half a meter: they are compatible with this production concept.

The process to generate the thin shells may introduce stress in the material. The characterization of the residual stress will be carried out based on the supply chain that will be chosen. In case, a proper annealing procedure may be studied to relax the stresses in the material.

During the manufacturing process, the internal and the external surfaces undergo grinding operations. The subsurface damage (SSD) is removed on the internal surface during the different polishing phases, but the treatment with a chemical etching could address the problem for both the internal and external surfaces at once. The assessment of this process will be the subject of further studies, based on experimental test campaign. As the strength of the glass depends on the surface quality,[8] the removal of SSD is particularly important for the mechanical modeling of the system. Higher glass strength simplifies the design of the LMA, increasing the resistance of the shell to launch loads. Moreover, it enables higher polishing force, with positive impact on the polishing speed. As the polishing time for large shell is not negligible, a faster polishing process will be very helpful in reducing the overall manufacturing time.

The thermo-structural model of the LMA is based on the materials compatible with fused silica. The list of these materials is reported in Table 2. In the current status, their mechanical properties are derived from literature and technical data sheets.

Table 2 Mechanical properties of the materials, as derived from literature and technical data sheet. CFRP data represent just a preliminary rough assessment. The ΔCTE respect to SiO_2 and the stiffness could be improved by a proper CFRP design.

	Young's modulus (GPa)	Poisson ratio	Density (t/m^3)	CTE (10^{-6} K^{-1})	Uncured viscosity (cPs)
SiO_2	70	0.17	2.201	0.51	NA
Ir	524	0.26	22.65	6.8	NA
CFRP	105	0.31	1.73	1.51	NA
Invar 36	141	0.29	8.05	1.3	NA
Invar 32-5	145	0.23	8.14	0.63	NA
Epoxy	2.1	0.35	1.2	61	225/425
Silicone RTV	0.004	0.45	1	230	3900

Given that the S3 and the final MM structure should match as much as possible the low CTE of fused silica, CFRP and INVAR are possible solutions. Owing to the high density of INVAR, the use of this material will be restricted to just mechanical couplings and components to be removed after the integration.

The connections of the MS to the S3 and to the MM structures are realized with adhesive. Two possibilities are under evaluation for the connection with the S3 (see Sec. 4). Epoxy could be used to increase the natural frequencies of the system, which could be helpful during the manufacturing process. On the other hand, better performances are expected with silicon (like RTV 566) for the decoupling from the external influences. The choice will be done taking into account the results of the characterization, in term of strength, shrinkage, and outgassing, of different adhesives. Moreover, special requirements apply for manufacturing process. The adhesive should be compatible with a wet environment (as the ones used in the grinding and the polishing phases) and should sustain thermal loads of some tens of degrees (as the one expected during ion-beam figuring phase).

A simple iridium-reflecting coating is assumed as a baseline for the T/M analysis, but multilayer coating could be envisaged to increase the effective area.

4 Shell Support System

The realization of thin shells is possible by taking advantage of the intrinsic stiffness of the monolithic shells and adopting an *ad hoc* integration concept based on a shell supporting structure (S3) jig. The dimensions of the S3 have to be coherent with the shell diameter and length. Nevertheless, to limit the number of S3 to be realized, the system should be designed to be compatible with some shells radially adjacent. The S3 has to be used for handling and supporting the shell in all the manufacturing steps (grinding, polishing, x-ray calibrations): it is designed to follow the shell up to the final integration in the SW. A similar system (called hereafter SSS) has been already designed and used for thin glass shells manufacturing.[9,10]

The S3 handling system should interface the different figuring equipment, limiting the deformations experienced by the shell. A sketch of the system is reported in Fig. 6. It is based on a metallic thin "comb," glued with a dedicated adhesive, which realizes a radial flexure at the connection between the MS and the external rigid structure. The goal is to minimize the radial forces on the MS. Loads are transmitted tangent to the MS wall, i.e., in the stiffer direction, minimizing MS distortions.

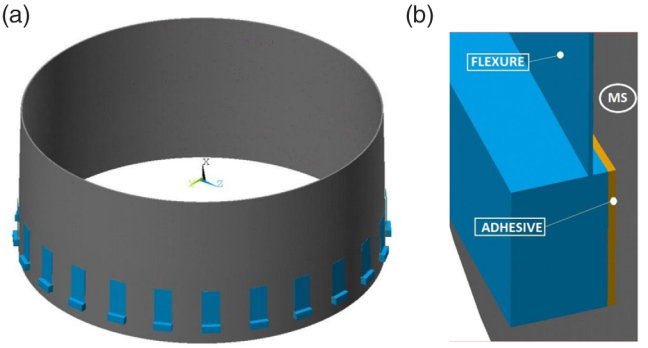

Fig. 6 Conceptual designs for the flexures, which are bonded on the glass surface and connected to the shell with the S3. (a) The flexures are azimuthally distributed around the smaller diameter of the semi-shell. (b) A layer of adhesive is foreseen for the fixation.

The flexures act in different ways with respect to the shell deformation scale. High-frequency deformations are not constrained by the flexures, whereas the low-frequency deformations are kept. To fix the shell to the S3, the shell is supported on a fixed number of points azimuthally distributed, which cause distortions on the same scale of the support spacing. While the shell is in this condition, it is bonded to the flexure system. If the number of flexure is doubled with respect to the number supporting points and their position is far from the support position, mechanical simulations show that the deformations almost disappear once the initial supporting system is removed and the MS remains sustained only by the flexures. On the contrary, in the assumption that during this integration phase a low-frequency deformation (as bilobe, trilobe) is introduced on the MS surface, it will be retained by the S3 system. These figure errors will be corrected during the manufacturing process and, as long as no springback is expected during the integration into the SW, their impact on the optical performances will be low. To this aim, the number of spokes should be sufficiently large to freeze the shell shape and only one flexure ring should be used.

The impact of the supporting scheme is evaluated with respect to the final effect on the MS shape: in a first phase, the constraints are moved from supports to flexures and in a second phase they pass from flexures to the SW. As stated before, the high-frequency errors, which could be introduced during the integration into the S3, are relaxed by the flexures, whereas the low-frequency errors are corrected during the manufacturing. Therefore, the optical performance degradation is very low. FEM simulations assume that the overall weight of the MS is distributed on three kinematic supports (three axial + three tangent constraints), plus $N-3$ axial forces. The total number of supports (N) ranges between 6 and 48, depending on the shell radius. Random forces are added to the nominal force distribution to allocate for supporting system manufacturing. The ranges of ± 0.01N and ± 0.01N have been considered. Ray-tracing evaluations are below $0.04''$ HEW for all the diameter range and with larger force error range.

As anticipated in Sec. 3, the connections of the MS to the S3 are realized with adhesive. Two possibilities are under evaluation. Epoxy could be used to increase the natural frequencies of the system, which could be helpful during the manufacturing process. For MS diameters ranging between 0.4 and 3 m, the MS frequencies are between 247 and 91 Hz if the bonding is realized with epoxy, whereas the MS frequencies are between 46 and 134 Hz with silicon. On the contrary, better performances are expected with silicon (like RTV 566) for the decoupling from the external influences and in terms of shrinkage. As the effect on the optical performances of the silicon adhesive is at least a factor 10 lower than the epoxy and the lowest natural frequency of the MS is still compatible with the manufacturing, the usage of silicon bonding is considered the baseline.

An "astatic" support (based on three kinematic supports + nine preloaded air-bearing pads) has been already realized and used for the integration of an old prototypal shell.[10] Figure 7 shows the current configuration of the astatic support available at INAF/OAB, whereas Fig. 8 shows an old shell during the integration into the SSS. The current SSS design will be revised in order to be compatible with the tighter requirements of the LMA shells. Two other major changes are foreseen. First, the double glass rings structure will be transformed in a stiffer system made of CFRP. Second, the radial flexure will be realized

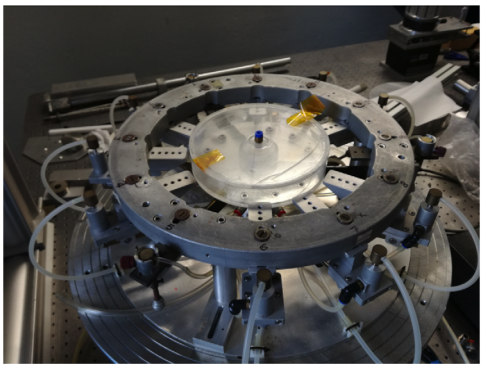

Fig. 7 The astatic support currently available at INAF-OAB: 12 supporting points are distributed in azimuthal direction. Three points at 120 deg are fixed, while the remaining can be preloaded considering the weight of the shell. To avoid frictions, the envelope pads are realized with a porous material so that the airflow prevents the drag.

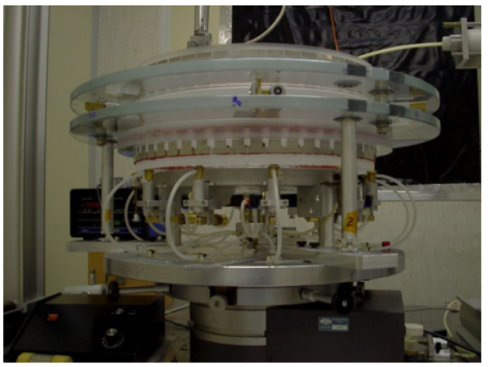

Fig. 8 The astatic equipment is used to support the shell during its fixation to the S3.

only on one side of the shell, near the edge to be fixed to the SW.

5 Manufacturing Steps

From a general point of view, the material removal rate decreases passing from grinding, polishing, and ion figuring. The lower the initial error at the entrance of each of the manufacturing steps, the faster will be the process phase. Nevertheless, the transition between the steps could be optimized taking into account their convergence rate and implication with respect to the next phases.

The optical surface to be figured ranges between 0.4 m^2 for the innermost shells and 6.2 m^2 for the outermost shells, in total around 342 m^2 for all the shells. Given the tight requirements to be achieved, the deterministic figuring is a well-known method to limit the manufacturing time and, as a consequence, the cost of the optics. On the other hand, the convergence of the figuring is driven by the accuracy of the metrological feedback. Given that the handling of the shells, in particular for the larger ones, could play an important role in terms of time and costs, the greatest challenge is to equip the different machines with dedicated onboard metrology systems. In this way, the shells should not be moved to metrological stations, with a consistent reduction of risks. The metrological feedbacks need to be fast and their accuracy should be adequate for the manufacturing step. The simplicity and the velocity of the setups will allow a constant monitoring of the process, while their accuracy will guarantee a fast convergence rate.

In this section, each of the manufacturing steps is briefly summarized. Their feasibility is discussed with respect to the results achieved in previous tests on prototypal thin monolithic shells.

5.1 *Grinding*

The geometry of a semishell is almost conical, with specific profiles along the shell meridians. To bring the optical surface near to the target, several tens of microns (as a minimum) should be removed from the surface, both along the azimuthal direction (errors in the roundness) and along the longitudinal directions. The out-of-roundness (OOR) correction and the profiles correction within some hundreds of nanometers are obtained by means of fine grinding process. Further corrections will be realized with direct polishing approach. From a general point of view, the impact of OOR error depends on the phase (in-phase or out-of-phase) of the residuals on the primary and on the secondary surfaces: their relative azimuthal orientation with respect to the optical axis could be used to compensate errors.

In general, an optical probe can be mounted directly on the lathe, allowing a pretty fast and accurate metrological system. Different optical probes, which guarantee high accuracy and low noise, are available on the market. This measurement setup can be used from the very first phase of the process, when the surface is rough.

So far, the fine grinding operations on thin monolithic glass shell has already been successfully proven. The activities were performed at LT Ultra Precision Technology GmbH by means of a high accuracy diamond turning lathe equipped with grinding wheels.[10,11] The setup of the grinding phase on thin shells is shown in Fig. 9. The correction of the OOR was stopped at around 1.5 μm peak-to-valley (PTV) errors.

To deal with larger MS (>1-m diameter), the same process could be adopted in the future, apart from what concerns the shell orientation, which could be changed to vertical condition. Depending on the grain size of the grinding wheel, different removal rates and microroughness are expected.[11] Therefore, the grinding sequence can be optimized, depending on the initial shell status.

5.2 *Polishing*

At the end of the grinding process and before the polishing phase, the SSDs on the surface have to be removed. Mechanical or chemical approaches could be used. While the chemical etching has not been yet investigated, a pre-polishing phase with the Bonnet tool has been successfully tested. It guarantees an efficient SSD removal. This DC removal does not change the profile's error but brings the microroughness below 5-nm RMS on the millimeter scale. At this level the surface become measurable with an interferometry approach. This pre-polishing process can be carried out directly on the grinding lathe by means of bonnet (not inflated but filled with rubber), see Fig. 10.[6] In addition, it can be operated directly with a standard Zeeko machine.[10–12]

Zeeko machine works on the concept of dwell time. It combines a rotary stage and six-axis robotic arm, with a complete control on the relative position of the tool and the surface: a finer correction of the residual azimuthal and longitudinal errors (down to the size of the tool print-trough) could be implemented.

Fig. 9 The shell on the lathe during the grinding phase.

As a drawback, the accuracy in the positioning is poor and the stages of the machine cannot be used directly for moving a probe for the metrology. Therefore a different metrological approach has to be used or, alternatively, an *ad-hoc* machine realized.

In general, the polishing of the internal surface shell is operated by combining the rotation of the rotary table and movement of the arm, in vertical and radial directions to follow the conical angle of the surface. Moreover, the bonnet tool is driven on the surface with a precession angle. As the machine works on the dwell time, the tool path is generated, taking into account the geometry of the surface and the error to be removed. Moreover, the tool patch follows the real relative alignment between the surface and the bonnet, in such a way that the applied offset is constant on the surface. The greater the offset applied toward the surface, the higher will be the removal rate.

Given that the shell is thin and changes shape when pressed, the maximum allowable offset has been derived in terms of maximum radial allowable deformation. This corresponds to a maximum load, which can be derived by mechanical simulations based on material strength. The velocity of the process could be higher in the future, when the data relevant to the material characterization become available.

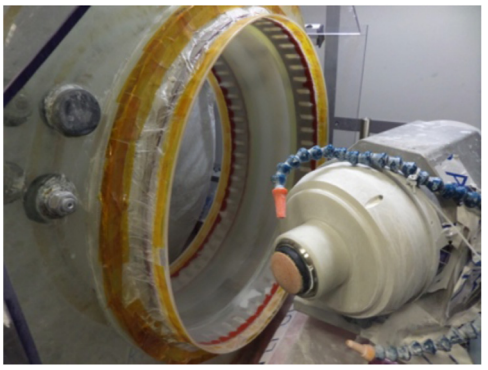

Fig. 10 The lathe is equipped with a bonnet tool. The CeO_2 is dispensed through the nozzle, reproducing the nominal Zeeko setup.

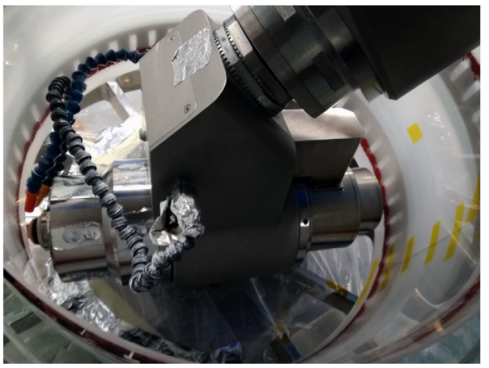

Fig. 11 The Zeeko IRP1200 equipped with the Bonnet R20 is used at INAF/OAB to polish an azimuthal segment of the shell#4. Given the relative size of the shell and of the robotic arm, the accommodation of the shell is not simple. The precession angle is reduced to 10 deg and set in horizontal direction. In this way the shell fits with few millimeters margin. The breakage that occurs on the lathe is visible on the right.

Figure 11 shows that the robotic arm of IRP1200 fits the shell#4 with a margin of a few millimeters.[11] Nevertheless, the working condition is very safe, as the approaching and the departure phases are based on the same machine language, which drives the polishing. The movements of the robotic arm are given in terms of the positions and orientations in the machine system reference. Once checked a first time, the operations can be realized automatically. This is a very safe condition with respect to the procedure adopted on the lathe, where the movements at the beginning and at the end of the machining had to be commanded in a manual way. The breakage of the shell#4 occurs during one of these phases.

The smoothing of the midfrequencies is achieved by means of pitch polishing (Fig. 12). This phase could be implemented on the same precision lathe by making use of a pitch tool device. To speed up the process and reduce the polishing time, an additional stage can be used to drive the tool with high frequency: while the shell rotates around the optical axis, the linear stage oscillates parallel to the surface of the shell.[11] The process can be optimized with regard to different parameters, such as the kind and the grain of the abrasive, the length of the movement, the pitch tool size, its oscillation frequency, and the force exerted (Fig. 13).

Fig. 12 The polishing phase with a pitch tool. The shell is mounted on the lathe with the optical axis in horizontal position. A liner carriage drives the oscillations of the pitch tool along the optical axis. CeO_2 slurry is distributed.

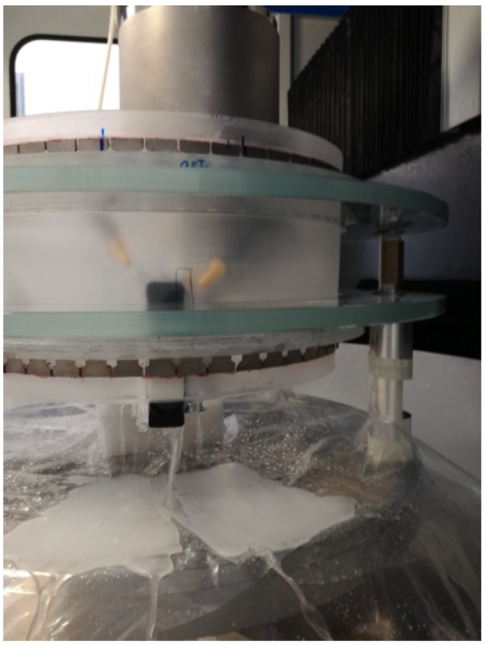

Fig. 13 The pitch tool equipped with TRizact 3M™ is fixed on the robotic arm of the Zeeko machine and the vertical carriage movement has been used to move the tool up and down.

Mechanical simulations confirm that the stress values during the process are not critical. The principal tensile stress peak is between 2.28 and 3.79 MPa for shell diameters ranging between 400 and 3000 mm. In the simulations, the pads width ranges between 20 and 60 mm for larger shell, while the applied pressure is set to 0.3 N/cm^2.

The target of this process is to achieve an error of about 1.3-nm RMS on spatial wavelengths between 2 and 10 mm and around 5- to 10-nm rms on longer scales. New kinds of abrasives, such as TRizact 3M, have been proved to be an effective solution: the usage of demineralized water instead of slurry is a great functional advantage in this kind of process and it reduces the cleaning time[6,13] (Fig. 14). Furthermore, it can be used down to the very last steps of polishing as it easily guarantees microroughness below 1-nm rms on the millimeter scales. With the correct settings in terms of pitch/abrasive/slurry parameters, the same kind of oscillating pitch tool can be used for the final superpolishing of the shell, aiming to reach a microroughness level of below 0.5-nm RMS.

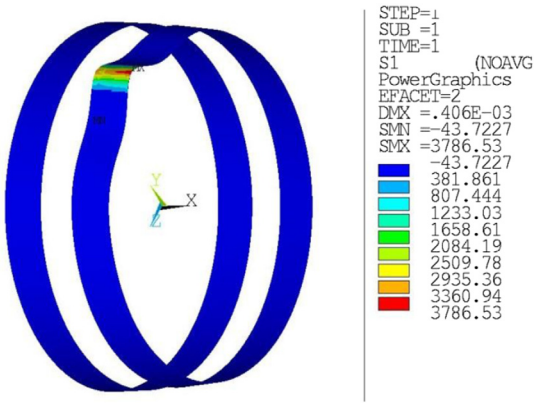

Fig. 14 Principal tensile stress contours for MS with 3-m diameter under the force exercised by a polishing pad (60 mm in width and with the same length of the section) with 0.3 N/cm^2 pressure.

5.3 *Ion-Beam Figuring*

At the end of the polishing activities, the accuracy on the longitudinal profiles is expected to be of the order of a few hundred nanometers PTV. This final error can be the sum of different factors, as the errors remain after the initial calibration of the stages and or the thermal effects. Moreover, due the floppiness of the shell, the standard direct polishing approach (e.g., not based on dwell time) could introduce errors in the surface.

As long as the surface microroughness is <0.5-nm RMS, the longitudinal low-frequency profile errors are theoretically correctable with an ion-beam figuring process, without degrading the microroughness.[14] This high-accuracy figuring process is operated by means of the large ion beam facility developed in the past years at INAF/OAB.[15,16] This facility, originally designed for large aspheric optics with diameters up to 1.3 m, has been upgraded, allowing the ion figuring of grazing incidence shells. To apply the ion beam correction, the shell is placed inside the chamber with the optical axis aligned as the gravity and a rotary table manages the shell rotation during the figuring.

A preliminary test on a close shell has already been performed. Figure 15 shows the setup inside the chamber. The test was a first assessment of the process, aimed to get a feedback on the temperature variations, on the microroughness variation, on the sputtering inside the shell, and on the shell shape. Owing to operational problems, the source was not stable during the figuring and the preliminary results need to be confirmed with further experiment. Nevertheless, it is worth emphasizing that no major showstopper has been identified.

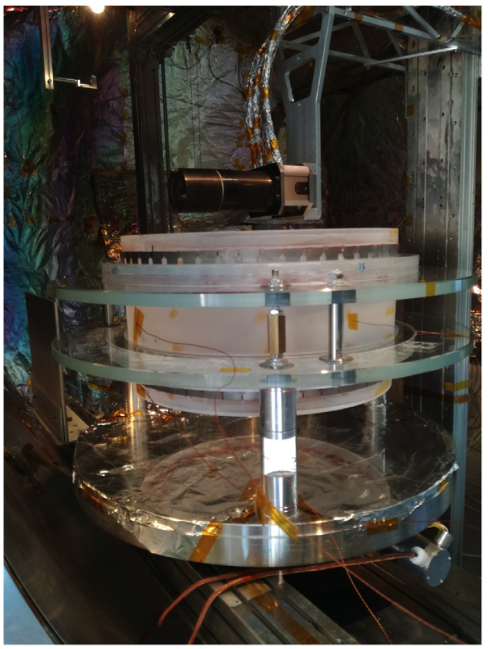

Fig. 15 The prototypal shell#4 in the ion beam chamber of the INAF/OAB during the first figuring test. Protection layers have been inserted on the ISW and uncoated witness glass samples distributed on the shell inner surface to monitor the sputtering process.

5.4 *Coating*

The coating is applied on the shell at the end of the polishing phase, while supported on the S3. From the operational point of view, the vacuum chamber for the deposition should be large enough to host the S3; no other constraints apply in the set-up. The combination of ion-beam figuring and the coating in the same vacuum chamber could be considered in particular for large diameter shells. This possibility could be cost effective, depending on the number of production lines and on the overall production schedule.

As long as the thickness and the stress of the deposit are kept constant along the shell surface, the symmetry of the closed-shell condition mitigates the deformations induced by the coating. In quasicylindrical geometries the tensioned coating effect is predictable. It mainly consists in edge effects, which damp toward the inner MS zone. So if a good coating homogeneity and repeatability is achieved (in terms of thickness and stress value), in principle it would be possible to correct the MS axial profile during grinding/polishing, to mitigate the elastic distortions induced by coating.

The coating stress represents a problem for all technologies under investigation for the Lynx mission; indeed, closed and quasicylindrical MS are less sensitive to such a problem.

Considering a deposit 35-nm thick tensioned with 350 MPa, the expected distortions are quite low (e.g., <0.1 μm radial displacement). Ray-tracing simulations show that the maximum contribution, expected for a shell of 1-m radius, is 0.45 HEW. The value of stress is quite conservative and the results can be scaled down linearly. Some very promising results have been achieved by alternating different materials in the coating deposition.[17]

The symmetry of the geometry will also help when the non-uniformity of the coating is considered. This is a major advantage with respect to segmented optics, where these deformations need to be avoided or compensated to prevent angular resolution degradations. For segments the same coating would contribute up to a few arcsecond degradation, depending on the radius and the thickness of the mirror segment. The first test on the coating will be carried out in the next phases.

5.5 *Intermediate X-Ray Calibrations*

Thanks to the mounting in the SSS, the x-ray calibrations of the shells can be performed, if needed, at different manufacturing stages. This is a very useful possibility, in particular, during the first part of the development phase.

As long as first x-ray measurements may be pursued after the polishing phase, they can be used to validate the metrological setup and the mounting concept itself. A cross-check can be done between the measured results and the expected HEW derived from the metrological data and mechanical simulations.

A second calibration run can be foreseen once the final ion-beam figuring process is done, when all the figuring activities on the shell are completed, with the goal to reach a sub-arcsecond angular resolution.

A final x-ray characterization could be envisaged before the final integration. Out-of-focus measurements could confirm the best relative rotation (around the optical axis) of the two semi-shells, which can be derived based on the metrological data. The defects, if any, could be concentrated in the same azimuthal area so that they can be masked with a minimum loss of effective area. On the contrary, it would be possible to optimize the throughput of the two semishells, compensating for the residual errors on the front with the ones on rear surface. Finally, the final x-ray calibration will assess the optical performances after the integration into the mirror structure of the entire set of MSs.

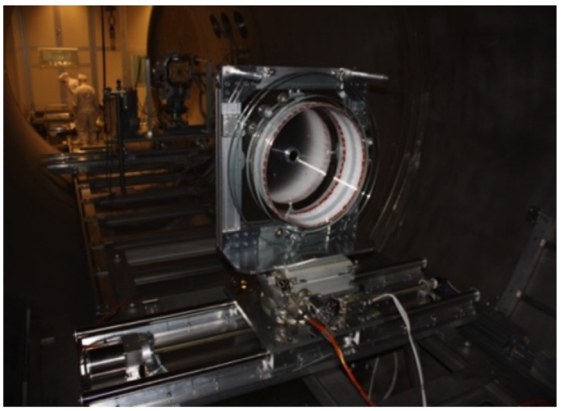

Fig. 16 The jig used to support the SSS with the shell#7 during the measurements @Panter in 2011.

A calibration of a thin, old prototypal shell in an intermediate stage of the polishing process has already been performed in 2011. The calibration was realized in Panter/MPE, and the setup is shown in Fig. 16.[10] Both in-focus and out-of-focus measurement were carried out. The interface between the SSS and the facility was realized with a simple frame of aluminum holding the SSS. In this configuration, the poor stiffness of the system could give rise to problems, as the distortions in the SSS introduce deformation in the shell. The problem was solved with the upgrade of the SSS (with an additional invar wheel interface) and the design upgrade of the holding system. The new setup is shown in Fig. 17, during the metrology in INAF/OAB.

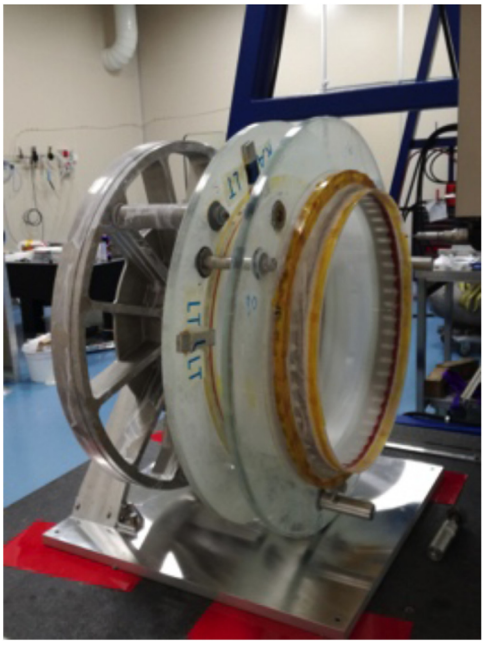

Fig. 17 The ISW, added to the SSS during the manufacturing of the shell#4, is interfaced to the new jig for calibration.

6 Integration into the Spoke Wheel and Mirror Module Design

Once ready, the shell has to be transferred into the SW. The semishells are bonded on the SW, while they are still integrated in the S3. From the operational point of view, front semishells (first reflection) are bonded on the smaller diameter, whereas the rear semishells (second reflection) are bonded on the larger diameter. Whereas the rear semishells can be nested from the bottom without any particular mechanical constraints, the front semishells are nested from the top. The current optical design is compatible with this scheme, as it respects the correct diameter sizing of consecutive semishell. In principle, no temporary bonding to additional structure is requested and the shell is transferred to the SW interfaces on the same side where the S3 is supporting the semishell. This helps to avoid undesired deformations.

The initial design of the SW foresees a bench with seven radial partitions. The number of spokes increases with the radius. They have a solid rectangular cross section and their width is variable with the radius, so that 10% geometrical obscuration is obtained (see Fig. 3). The SW is made of CFRP, with a thickness in axial direction of 250 mm and with a mass of 348 kg. As anticipated, in the current design, a conservative approach is used with respect to the CFRP mechanical properties. All the performances directly affected by the stiffness of MM structures will benefit by the improvement expected from the optimization of the composite material parameters.

With respect to the connections between the MS and the spokes, the preliminary results show that proper connectors giving some radial decoupling between SW and MS are necessary. In this way, the thermal effects due to the materials' CTE mismatch will be mitigated. Similar benefits also apply to gravity release effects and to stress peaks in MS at SW connections. On the other hand, the decoupling should not be too large to avoid springback phenomena when MS constraints pass from S3 to the SW.

The MS integration is foreseen in vertical condition, with the gravity in axial direction and parallel to the optical axis. It will be carried out as a "steady mass" process: the SW will be loaded by dummy masses to mimic the weight of the missing MSs. The dummy masses will be removed after the integration of each MS, so that the overall mass and the related SW deflections do not change along the whole process. During the integration phase, an excessive elastic deflection of the SW should be avoided, as it degrades the performances of the LMA at the gravity release. A stiffer SW or a dedicated supporting scheme counteracts the axial gravity effects. A preliminary scheme based on astatic levers is considered: 12 astatic levers at the SW inner ring (1-m diameter) and 45 astatic levers + 3 axial/azimuthal supports 120 deg spaced at the outermost ring (3-m diameter). The SW drawing and the astatic levers scheme are shown in Fig. 18. If the MM x-ray calibrations are carried out in the same configuration used during the integration (with axial gravity + supporting forces at work), in principle, the gravity has no effect. On the contrary, the lateral gravity is a disadvantageous condition in terms of HEW degradation but the achieved results are encouraging, as the optimization of the SW design and supporting system can improve the result further.

Gravity in axial or in lateral direction has been applied to the MM continuously supported in axial and tangent direction (radial free) at the outer ring. These loadings do not correspond to any effective configuration envisaged during the integration/testing process, but they are representatives of the intrinsic SW stiffness. The radial (U_R) and axial (U_A) displacement contours relating to the axial and lateral gravity are reported in Figs. 19 and 20, respectively.

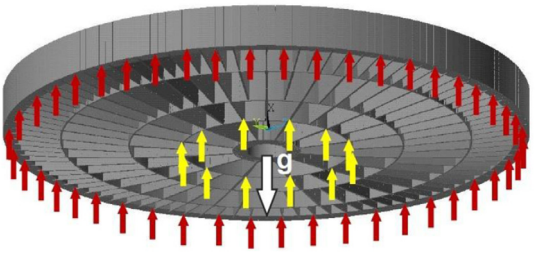

Fig. 18 Supporting scheme during the integration phase.

Gravity release assessments refer to the above-described integration procedure: a certain number of supporting forces are envisaged during the integration phase to mitigate the SW axial gravity deflections. Figures 19 and 20 show the axial and radial displacements of the SW at the gravity release. The SW deformations, mitigated by proper MS–SW connectors, represent the major source of MS distortions.

The impact of the reference temperature gradients has been analyzed with kinematic constraints applied to the MM to allow thermal expansions. Three axial and three azimuthal

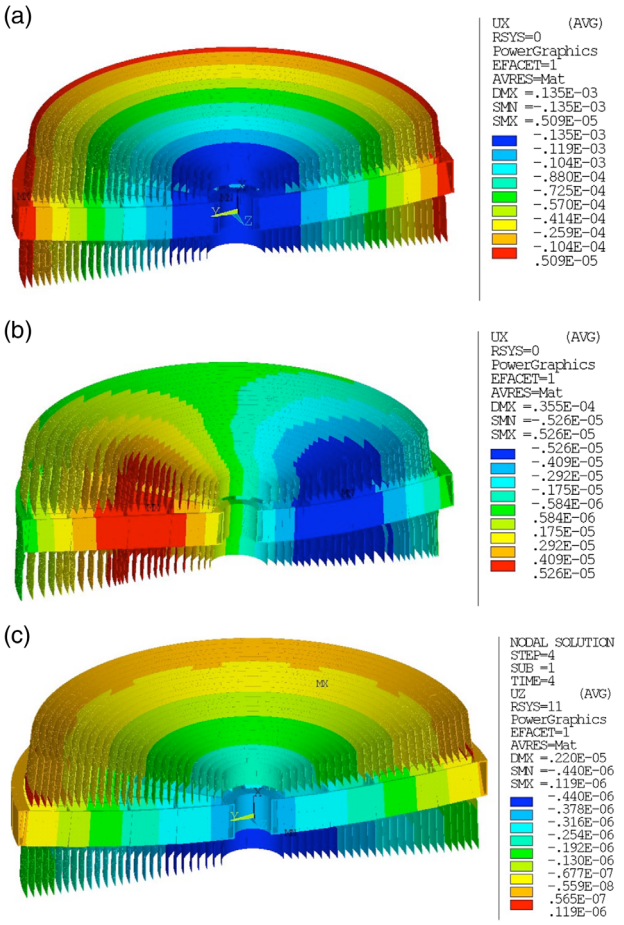

Fig. 19 (a) Axial gravity, (b) lateral gravity, and (c) $\Delta T = +1°C$ just on SW. U_A contour is quoted in meters.

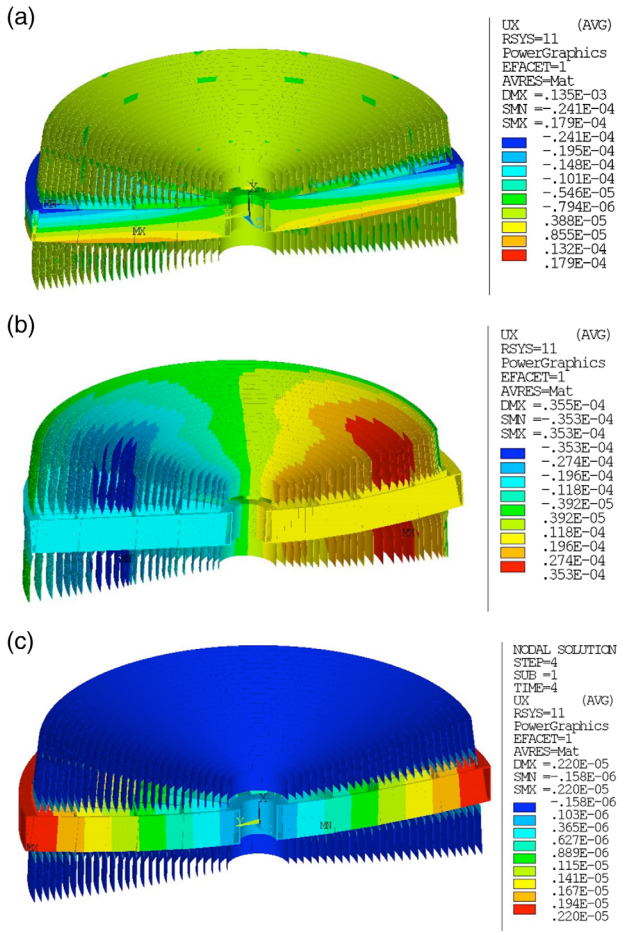

Fig. 20 (a) Axial gravity, (b) lateral gravity, and (c) $\Delta T = +1°C$ just on SW. U_R contour is quoted in meters.

rigid constraints, 120 deg spaced at outer ring, were assumed. Radial, lateral, and bulk gradients were considered. Here, U_R and U_A contours are shown in Figs. 19 and 20 for a bulk gradient of 1°C.

Table 3 reports a summary of the ray-tracing results achieved at different conditions. The MM is simulated by means of 14 "optical MS" radially distributed, having the real geometry, and 13 "dummy MS." Each of these last dummy MS is equivalent in terms of stiffness and mass to the whole MS set between two optical MSs, so that they are representative of the whole MM. Just optical MS are used in the optical postprocessing of FEA. Further improvements in the structural performances are expected in future iterations between mechanical and optical designs.

The MM frequencies are also computed assuming two extreme support conditions. In the first case, continuous radial and tangent supports at the outer SW ring are considered, whereas in the second case only three axial and three tangent supports at the outer SW ring are assumed. The results, achieved with rigid constraints, are reported in Table 4. Based on the final frequency requirement, a more realistic support condition (for instance usage of provisional supports at launch) will be defined.

The launch gives rise to severe loadings in terms of tensile stresses in the MS. Tensile stress peaks related to quasistatic loads at the SW interfaces are assessed in Table 5. Quasistatic loading combinations were applied. The radial, the tangent and

Table 3 Gravity, reference temperature gradients, and gravity release—MM ray tracing results. Results are given at nominal focus (NF) and at BF. ΔTU, uniform temperature change; TGA, axial thermal gradient; TGL, longitudinal thermal gradient; TGR, radial thermal gradient; and ΔTS, temperature mismatch between ISW and MS.

	HEW (arc sec) NF	HEW (arc sec) BF	Δf (mm)
Gravity (axial)	1.17	1.01	−0.081
Gravity (lateral)	2.00	2.00	
Gravity release	0.38	0.26	−0.041
Thermal loading **ΔTU**	0.26	0.15	+0.03
Thermal loading **TGA**	0.06	0.03	−0.01
Thermal loading **TGL**	0.55	0.55	
Thermal loading **TGR**	0.20	0.20	−0.019
Thermal loading **ΔTS**	0.37	0.22	+0.04

the axial forces at connectors between SW and MS were derived in four optical MSs These correspond to the largest MS (in terms of ϕ_{IP}), respectively, connected to 12/24/48/96 spokes. A detailed FEM of each MS in kinematic constraint conditions was implemented. SW interface reactions and quasistatic gravity loads were applied, so that loadings were self-balanced (null reaction forces at kinematic constraints). Each SW interface reaction force was spread on a square load-print 10 mm × 10 mm. The SW bending deflections transmit radial displacements to the MS, increasing the local bending stress in the shell. A further optimization of the SW stiffness is possible. The stress levels reported in Table 5 are demanding but are not prohibitive. Proper design optimization is needed to reduce

Table 4 MM frequencies, continuous support, and kinematic mount. The effective mass is the mass moving at the relevant frequency.

	Continuous support		Kinematic mount	
	Freq. (Hz)	Eff. mass (tons)	Freq. (Hz)	Eff. mass (tons)
Axial direction (*X* axis)	35.4	2.00 (78%)	54.3	1.77 (69%)
Lateral direction (*Y* axis)	27.1	0.04 (1.4%)	93.3	0.74 (29%)
	63.7	1.26 (49%)	97.8	0.64 (25%)
Lateral direction (*Z* axis)	27.1	0.04 (1.4%)	93.3	0.74 (29%)
	63.7	1.26 (49%)	97.8	0.64 (25%)
Rotation around *X*	34.2	1.5	34.3	1.49
		2	69.8	0.54
Rotation around *Y*	27.1	0.80	93.3	0.10
Rotation around *Z*	27.1	0.80	93.3	0.10

Table 5 MS stress peaks under load combinations (MPa).

MS #ID	ϕIP/2 (mm)	Spoke number	Tensile stress peak (MPa)
142	1472.2	96	5.35
119	1104.4	48	6.44
082	701.8	24	9.07
040	399.3	12	6.37

the stress level and risks on the basis of a reliable assessment of SiO_2 strength after the experimental campaigns.

7 Error Budget

The top-level error budget for the mirror assembly realization is reported in Table 6. The optical design foresees 0.3 arc sec on-axis HEW at 1 keV on a defined focal plane position. Taking into account the contribution of the diffraction of the different shell weighted for their effective area, the total HEW is 0.31 arc sec.

The sensitivity analysis, reported in Sec. 5, returns contributions between 0.03″ and 0.55″ (for 1°C DeltaT), depending on the thermal load distribution. This gives confidence that, with a dedicated thermal control, the T/M contribution can reasonably be limited to 0.2 arc sec. In addition, the effect of the gravity release has been evaluated through FEM simulations. The current contribution (0.26 arc sec) is derived with a preliminary design of the SW structure. It could be decreased working on materials, increasing the CFRP Young's modulus to raise the SW stiffness, and on the optimization of mechanical design, refining the design of the SW structure and its connection to the MS.

Table 6 Error budget.

Optical configuration			0.31
	Design	0.3	
	Diffraction	0.09	
On-orbit loads			0.33
	Thermal	0.2	
	Gravity release	0.26	
Shell manufacturing			0.24
	Metrology	0.05	
	Front mirror figure error	0.15	
	Rear mirror figure error	0.15	
	Shell supporting system	0.05	
	Coating	0.1	
Integration			0.18
	Alignment error	0.15	
	Bonding	0.1	
FINAL HEW			0.55

The reduction of the T/M contribution will increase the margin for the shell manufacturing, which is now set at 0.24 arc sec. This error is distributed between different terms. (1) Simulations return the coating contribution. As reported in Sec. 3, assuming a value of tensile stress (350 Mpa, for an Ir coating 35-nm thick), the error contribution ranges between 0.24 and 0.45 arc sec HEW. Given that this stress value is very conservative with respect to the reality, its reduction is feasible leading to an impact of the order of 0.1 arc sec HEW. The symmetry of the geometry will also help when the nonuniformity of the coating is considered. (2) The accuracy of the metrology during the manufacturing process and during the tests limits the performances of the final optic. The error contribution is set to 0.05 arc sec. In principle, reference mirrors and lens can be realized down to 5-nm rms accuracy. Moreover, interferometry setup, a proper choice of the ground equipment materials, and a good thermal control of the environment (0.2°C) can guarantee a repeatability of the same order. (3) The handling and the manufacturing of the shells are realized with dedicated supporting systems. The analyses have shown that the SSS acts differently on the low and high spatial frequency errors. For instance, if we consider the MS deformations induced by MS supports before the connection to SSS, we see that the nominal supporting forces deform the shell with high spatial frequency errors, which are relaxed by the flexures. On the contrary, the errors in the supporting forces generate low-frequency errors, which are kept by the system. As long as they are corrected during the figuring of the shell and no significant springback is expected after the shell integration into the SW, the contribution of the supporting system can be very low. Preliminary analysis on the SSS returns a 0.05-arc sec contribution. (4) The error term related to the optical surface error is set to 0.15 arc sec for both the front and the rear surfaces. (5) Main terms contributing to this error are the longitudinal profile, the azimuthal and the microroughness errors. (6) Numerical simulations have shown that by limiting the profile error to around 10-nm rms, the expected contribution is kept below 0.1 arc sec HEW. Given that azimuthal error impact scale down with the focal length, a 200-nm PTV azimuthal error would contribute 0.05″ in HEW. Microroughness values around 0.2 to 0.3 nm (within the standard polishing capabilities) would return negligible contribution in terms of HEW.

The error term related to integration (0.18 arc sec) is split in two main contributions. The alignment term is dominated by the tilt between the optical axis of the front and the optical axis of the rear surfaces. While the rotation around the optical axis has no effects, the contribution of displacement errors can be kept <0.04 arc sec, if an accuracy of few microns is reached. Given that only one side of the semishell has to be bonded to the SW, the transfer will be relatively easy, with reduced distortion possibilities. There are several space-qualified epoxies in the market, which can guarantee very low shrinkage. As the number of the shell to be integrated is limited to few hundreds, the integration time per shell is not driven by the schedule. As a consequence, there are no limitations in the epoxy selection based on the curing time and the setup of a reliable and smooth bonding process is possible.

8 Results on Prototypal Shells

The realization of thin, fused silica monolithic shells started as part of the feasibility study of the Wide Field X-ray Telescope mission concept.[9] For that mission concept, three x-ray MMs based around 60 shells were needed to reach a total effective area of 1 m^2. In each module, the shell diameter was ranging between 300 and 960 mm, with a focal length of 5 m. To limit the weight of the mirrors, the shell thickness was in the 2- to 3-mm interval. The main difference with respect to the current design was the fact that these shells were almost double conical. In this case, the front and rear optical surfaces were joined at the IP.

The general viability of the direct polishing approach on thin glass shells was demonstrated in 2012 (TRL3), using a process pretty similar to one described in previous paragraphs. A prototypal shell was manufactured (shell#7), with a polynomial optical design and with a small aspect ratio. Starting from a raw, grinded fused silica shell produced by HERAEUS (Germany), a double-cone shell was precisely grinded by LT-Ultra (Germany). A deterministic polishing and figuring process was then applied by means of IRP600 Zeeko machine based on bonnet polishing in order to impose the polynomial Wolter-like profile adopted for WFXT. Then, a pitch superpolishing process was implemented using a dedicate pitch tool mounted on the IRP600 arm. An intermediate x-ray calibration was carried out at Panter/MPE (with TRoPIC detector) to cross-check the performances with the available metrological data. To follow as much as possible the focal plane curvature, the images have been acquired at the best focus (BF) of each angular position. The x-ray data (0.93 keV) have been collected on axis, at 10′, at 20′, and at 30′ off-axis angles. As expected, the measured HEW was quite flat across the FOV. The values recorded vary from 17.8″ on-axis up to 23.7″ at 30 arc min off-axis.[10] The ray-tracing simulations based on metrological data can explain the x-ray calibration results with the following error terms. The low-frequency longitudinal profile errors contribute 6″ to the final angular resolution on the on-axis data. The HEW increases to 8″, adding the OOR contribution. It reaches 12″ considering the tilt between the optical axes. The measured HEW is reached considering the longitudinal profile midfrequency contribution. The surface microroughness, measured around 1-nm RMS, brings a negligible contribution at low energy. The results of this intermediate x-ray measurement showed that the major drivers for improving the shell optical quality were the correct reciprocal alignment of the optical axis of the two reflecting surfaces and the reduction of the midfrequency errors. Unfortunately, the shell was damaged during the postcalibration measurement activities and the programmed final polishing on this shell could not be carried out.

The development of a new shell (shell#4) started in 2013, based on a standard Wolter-I design. To overcome the problems faced with shell#7 and to reach sub-arc sec performances, the production flow of the shell has been partially modified, increasing the stiffness of the SSS by means of an Invar spoke wheel (ISW). The polishing of the shell was not completed mainly due to lack of funds. The work on this shell has been restarted in 2017, thanks to a dedicated founding program of the Italian Space Agency (ASI). The summary of the activities and the final status of the shell is reported in Ref. 11. The operations on the shell restarted from the grinding phase, followed by a bonnet polishing to reduce the SSD. This process has been applied directly on the lathe with a dedicated mixing device at controlled temperature was purchased for the slurry distribution. Unfortunately, the shell was broken due to a wrong carriage movement, during the metrological phase of the last run of bonnet polishing. The breakage passes through the shell height completely. An UV curing adhesive was used to fix the shell. Owing to the shell fracture, it was not possible to operate on all portions of the shell, as the pitch tool could be damaged passing above the fracture. Limited test are possible on an azimuthal portions of the shell. In 2018, the test activities restarted by means of the available equipment in INAF/OAB laboratories, with the aim to complete the figuring of an azimuthal segment. The Zeeko IRP1200[11,18] was used both for Bonnet polishing and for the pitch polishing. The machine geometrical constraints limit the convergence rate of the process. Even if this working configuration is not adequate for an evaluation of the process duration, it is suitable for a preliminary assessment of the ion-beam figuring process. The microroughness is evaluated with MicroFinish Topographer 10× on the scale of 1 mm, whereas a new setup, based on the interferometry approach, is used for the longitudinal profiles acquisition. The collimated beam passes through a cylindrical lens and is reflected with a flat mirror at 45 deg before hitting an azimuthal section of the shell. Profiles are extracted from the interferometer map, whereas OOR are acquired on a rotondimeter.

9 Plans for the Future

The roadmap for the technology maturation is defined taking into account the TRL milestones requested for the Lynx Mirror Assembly Trade. The definitions specify the angular resolution and the fidelity with respect to the final hardware of the breadboards.

TRL3 (2018, 3″ HEW) is achieved with the complete test of the figuring process on a section of shell. In particular, this includes the IBF, as this step of the process has never been tested on a closed shell. The demonstration will be realized on a sector of the broken shell#4.

The manufacturing of a complete semishell is expected at TRL4 (2020, 1.5″ HEW): a single-reflection shell will be fully figured, polished, superpolished, and corrected by means of ion-figuring. Moreover, the transfer to a breadboard ISW will be verified, proving that the shell's optical quality is not degraded. If the feasibility of transfer is demonstrated, the main maturation step of full shell technology is achieved. The remaining part of the roadmap is expected to run smoothly, being just a repetition of the concept for larger shells.

TRL5 (2024, 0,75″ HEW) is achieved with a composition of larger semishells. In this phase, the coalignment between semishells will be tested. An alignment concept similar to the one of AXAF could be implemented. Depending on the available funding, the test could be realized on larger diameter shells (the maximum diameter settable at Marshall/XCRF is 1.4 m). As new equipment would be necessary for the manufacturing of the shells, as an alternative, the breadboard could be realized by maintaining almost the current sizing, but the practicability of the large MS production should be proven. Furthermore, the feasibility of the supporting system should be verified trough metrological approach.

The supply chain for the provision of the raw shells, compatible with a diameter of up to 3 m, will be fixed in the following months, and the new semishell will be purchased to start the breadboard manufacturing activity. In parallel, the characterization of the materials will be performed in order to get proper

inputs for a reliable structural analysis. The internal stress of the raw MS is necessary for a trustworthily simulation of the spring-back after the integration into the mirror structure. The strength of the SiO_2 should be characterized for assessing the environmental loads during manufacturing and at launch. In particular, these tests should follow the identification of a reliable chemical etching process to reduce the SSD on both sides of the shell. The resistance of the glass is expected to increase, with benefits for the structural analysis and the manufacturing process optimization.

10 Conclusions

Lynx is an x-ray mission concept based on mirror assembly with superb imaging capabilities, large effective area, and extended FOV. The mirror assembly realization is a very challenging technological task. Several approaches are being considered to meet the required mirror accuracy. The full shell concept is based on monolithic fused silica shells. Given the mass constraints, their thickness should be <4 mm for MSs up to 3-m diameter.

In this paper, we have presented the optomechanical design of the mirror assembly, which fulfills the requirements. The design is based on a central SW, holding the semishells of front and rear surfaces on opposite sides. The simplicity of the design is boosted by the adoption of monolithic shells, so that the number of items to be realized is limited to few hundreds. The top-level error budget has been discussed in relation to the allocations settable by the preliminary optical and mechanical evaluations. The proposed manufacturing process, based on direct polishing and ion-beam figuring, is compliant with the requested tolerances. A support structure is being finalized to sustain the semishells during the figuring and polishing operations and to manage the handling until their integration into the telescope structure. The design will be based on the experience with the SSS, which has been used so far for double-conical thin shells.

The preliminary results achieved so far on a breadboard shells have been discussed. Owing to a breakage on one section of the shell currently under development, the polishing configuration is not straightforward as the azimuthal symmetry guarantees for full shells. Nevertheless, the IBF facility available at INAF/OAB is in use for testing the ion-beam figuring process on closed shells for the first time. With respect to the future plans, the technological maturation roadmap is delineated in terms of milestones, defined in accordance with NASA TRL definitions. The main technological achievement is expected in 2 years, with the realization of a complete thin semishell and its transfer in a breadboard SW.

Acknowledgments

We thank the Italian Space Agency (ASI) for its support with a contract focused on glass shell development for x-ray optics (Accordo ASI INAF 2015-041R.0 - Glass Technology for the next generation x-ray optics). We would also like to thank NASA Headquarters for their support in the study of the Lynx mission.

References

1. S. L. O'Dell et al., "Toward large-area sub-arcsecond x-ray telescopes II," *Proc. SPIE* **9965**, 996507 (2016).
2. J. A. Gaskin et al., "Lynx mission concept status," *Proc. SPIE* **10397**, 103970S (2017).
3. L. P. Van Speybroeck et al., "Performance expectation versus reality," *Proc. SPIE* **3113**, 89–104 (1997).
4. C. T. DeRoo et al., "Deterministic figure correction of piezoelectrically adjustable slumped glass optics," *Proc. SPIE* **10399**, 103991M (2017)
5. W. W. Zhang et al., "Monocrystalline silicon and the meta-shell approach to building X-ray astronomical optics," *Proc. SPIE* **10399**, 103990S (2017)
6. M. Civitani et al., "Lynx optics based on full monolithic shells: design and development," *Proc. SPIE* 1069911 (2018)
7. R. C. Chase and L. P. van Speybroeck, "Wolter–Schwarzschild telescopes for X-ray astronomy," *Appl. Opt.* **12**, 1042–1044 (1973)
8. C. A. Klein, "Characteristic strength, Weibull modulus, and failure probability of fused silica glass," *Opt. Eng.* **48**(11), 113401 (2009)
9. L. Proserpio et al., "Design and development of thin quartz glass WFXT polynomial mirror shells by direct polishing," *Proc. SPIE* **7732**, 77320D (2010).
10. M. Civitani et al., "Thin glass shell oriented to wide field x-ray telescope," *Proc. SPIE* **8443**, 84430Q (2012).
11. M. M. Civitani et al., "Thin fused silica shells for high-resolution and large collecting area x-ray telescopes (like Lynx/XRS)," *Proc. SPIE* **10399**, 103990W (2017).
12. D. D. Walker et al., "Precessions process for efficient production of aspheric optics for large telescopes and their instrumentation," *Proc. SPIE* **4842**, 73–84 (2002).
13. M. M. Civitani, J. Hołyszko, and G. Vecchi, "Probing 3M™ Trizact™ abrasive pads in the polishing and super-polishing phase of fused silica," *Proc. SPIE* **10706**, 107063K (2018);
14. W. Liao et al., "Morphology evolution of fused silica surface during ion beam figuring of high-slope optical components," *Appl. Opt.* **52**, 3719–3725 (2013)
15. M. Ghigo et al., "Development of a large ion beam figuring facility for correction of optics up to 1.7 m diameter," *Proc. SPIE* **7426**, 742611 (2009).
16. M. Ghigo et al., "Ion figuring of large prototype mirror segments for the E-ELT," *Proc. SPIE* **9151**, 91510Q (2014).
17. D. M. Broadway et al., "Achieving zero stress in iridium, chromium, and nickel thin films," *Proc. SPIE* **9510**, 95100E (2015).
18. G. Vecchi et al., "A bonnet and fluid jet polishing facility for optics fabrication related to the E-ELT," *Mem. S.A.It.* **86**, 408 (2015).

Marta M. Civitani is a technologist researcher at INAF—Brera Astronomical Observatory in Italy. She received her MS degree in physics from the University of Milano (Italy) in 1999 with a thesis on observational cosmology. Afterward, she spent several years working in aerospace companies as a test engineer for scientific payloads. She obtained a PhD in astronomy and astrophysics in 2012 from the University of Insubria (Como, Italy). Her current research interests include the design, development, implementation, and calibration of x-ray optics for astronomical and ground-based telescopes.

Giancarlo Parodi is an independent consultant in optomechanical and structural engineering as partner of the company BCV Progetti Srl. He received his MS degree in structural engineering from Polytechnic University of Milan in 1983. In more than 30 years, he designed and analyzed several instruments and components for astronomy from ground and in space, cooperating with research institutes and industry to develop new optical components technologies. He co-authored more than 60 technical papers on optical engineering projects.

Biographies of the other authors are not available.